

# Melting curve of correlated iron at Earth’s core conditions from machine-learned DFT+DMFT

Rishi Rao and Li Zhu\*

*Department of Physics, Rutgers University, Newark, New Jersey 07102, USA*

(Dated: January 6, 2026)

Reliable constraints on iron’s melting curve at Earth’s inner-core boundary require accurate finite-temperature electronic correlations, yet DFT+DMFT calculations remain too costly for large-scale thermodynamic sampling. Here, we develop a machine-learning accelerator for charge self-consistent DFT+DMFT by training E(3)-equivariant graph neural networks to predict the local self-energy and Fermi level from atomic environments, providing an efficient warm start to the DMFT self-consistency loop. Using high-throughput data for Fe, FeO, and NiO, we obtain a 2–4 times reduction in DMFT iterations. Leveraging this improvement, we generate correlated energies and forces for Fe at core pressures, train a neural-network interatomic potential, and determine the melting curve via two-phase coexistence simulations. We obtain a predicted melting temperature of 6225 K at 330 GPa.

Correlated electron systems occupy a central place in modern condensed-matter physics. Their rich behaviors, including metal–insulator transitions [1, 2], unconventional magnetism [3, 4], and high-temperature superconductivity [5–7], arise from strong local interactions, particularly in transition-metal compounds where lattice, spin, orbital, and charge degrees of freedom are tightly intertwined [8, 9]. Understanding how this interplay governs electronic properties across pressures, temperatures, and compositions remains one of the major challenges in computational materials physics and is essential for problems spanning functional oxides to materials under extreme pressure and temperature conditions.

Fe at the conditions of Earth’s core exemplifies the challenges of simulating correlated systems [10–12]. The melting curve of Fe at hundreds of gigapascals controls the temperature at the inner-core boundary (ICB) and thus constrains the thermal history and dynamics of our planet, yet experimental determinations at these pressures are extremely challenging and theoretical predictions span a broad range of temperatures. While recent experiments have begun to converge on values near 6200 K at ICB pressure [13–15], theoretical predictions from density functional theory (DFT) calculations remain scattered, with discrepancies often exceeding 1000 K [16–25]. A fundamental limitation of standard DFT approaches is their inadequate treatment of dynamical correlations in Fe [10–12]. Under core conditions, hexagonal close-packed (hcp) Fe and body centered cubic (bcc) Fe retain their Fermi-liquid character while fcc Fe displays markedly non-Fermi liquid behavior, with relative free energy differences changing significantly with temperature [11]. Incorporation of these correlation-induced differences are neglected with conventional exchange-correlation functionals, but must be included for accurate simulations of liquid phases.

Dynamical mean-field theory (DMFT), which captures local correlations in a fully dynamical and non-perturbative manner [26], offers a path forward. Coupled

to DFT, it allows for realistic simulations of correlated materials by taking into account effects such as quasi-particle renormalizations, and provides access to electronic and thermodynamic properties such as spectral functions and finite-temperature phase diagrams [27]. However, this power comes at a substantial computational cost. Each DMFT calculation requires repeated solution of the quantum impurity problem until impurity and lattice occupations become consistent. Determining a melting curve requires sampling thousands of large-scale atomic configurations through molecular dynamics, a task that has remained prohibitively expensive within DFT+DMFT.

Recently, machine learning has begun to be explored as a way to reduce the cost of DMFT calculations, for example through surrogate impurity solvers, learned corrections to approximate Green’s functions, and data-driven models trained on simplified parameter spaces [28–31]. While these studies demonstrate that key DMFT quantities can often be approximated efficiently in selected settings, most existing approaches have been confined to model Hamiltonians or narrow material classes, and the learned targets are not always constructed to respect the analytic structure and symmetry constraints required in realistic DFT+DMFT workflows. It therefore remains unclear whether machine learning can provide a robust, physics-consistent acceleration of DFT+DMFT for correlated solids with the accuracy needed for thermodynamic predictions, particularly under the extreme conditions relevant to Earth’s core.

In this work, we demonstrate that embedding physical constraints into machine-learned self-energies enables, for the first time, systematic DFT+DMFT determination of the iron melting curve at core conditions. Our approach exploits the analytic structure of the self-energy: we decompose it into a static high-frequency limit  $\Sigma(\infty)$  and a frequency dependent term  $\Sigma(i\omega)$ , represented compactly through Legendre coefficients, with each component predicted by E(3)-equivariant graph neural networks that

respect the point-group symmetry of the local atomic environment. This physics-informed representation reduces the learning problem to smooth, real-valued targets while preserving the causal structure essential for DMFT self-consistency [31].

The resulting model accelerates DMFT convergence by a factor of two to four across Fe, FeO, and NiO, enabling high-throughput generation of correlated electronic structure data. We leverage this capability to train a machine learned interatomic potential (MLIP) for iron and perform two-phase coexistence simulations spanning 307–352 GPa. Our predicted melting temperature of 6225K at 330 GPa agrees well with the recent experimental measurements [13–15], providing strong validation that large-scale molecular dynamics (MD) simulations using DMFT-based MLIPs are viable for phase-equilibrium calculations in planetary interiors.

Within DFT+DMFT, electronic correlations enter entirely through the local self-energy. For each correlated atom and orbital, the DMFT loop determines a frequency-dependent self-energy  $\Sigma(i\omega_n)$  that, together with the noninteracting lattice Green’s function, gives the electronic structure and thermodynamic properties of the crystal. The real part of  $\Sigma$  controls band renormalization and shifts, while the imaginary part governs lifetimes, scattering rates, and the appearance of incoherent spectral weight. In practice, for every crystal structure and thermodynamic state point  $(T, P)$  one must find a fixed point of the DMFT equations at which the impurity and lattice quantities (such as occupancies and local Green’s functions) become consistent, yielding a converged self-energy  $\Sigma$ .

Formally, this converged self-energy is a functional of the local environment: it depends on the atomic configuration, the chemical composition, and the thermodynamic parameters, as well as on the choice of correlated subspace and interaction parameters. In this work we make this viewpoint explicit and seek an approximate, parameterized functional  $\Sigma^{\text{ML}}[\mathcal{S}](i\omega_n)$  that maps a given structure  $\mathcal{S}$  (including atomic positions, species, and volume) to an orbital-resolved local self-energy close to the DMFT fixed point. The goal is not to replace DMFT entirely, but to provide an initial approximation  $\Sigma^{\text{ML}}$  that lies close enough to  $\Sigma$  such that this fixed point may be reached more rapidly.

A naive strategy would be to train a neural network to output  $\Sigma(i\omega_n)$  directly on a discrete Matsubara frequency grid. This is undesirable for several reasons. First, the DMFT self-energy is complex-valued and, when obtained from quantum Monte Carlo impurity solvers, can be noisy at high frequencies. Second,  $\Sigma(i\omega_n)$  obeys strict analytic constraints: it is a causal function with a well-defined high-frequency expansion,  $\Sigma(i\omega_n) = \Sigma(\infty) + \mathcal{O}(1/i\omega_n)$  [32], and its imaginary part has definite sign on the imaginary axis. Direct regression on a large set of complex values risks violating these

constraints unless they are enforced explicitly.

Instead, we adopt a physics-constrained representation tailored to the analytic structure of the self-energy. The real part of the self-energy approaches a frequency-independent limit as  $\omega_n \rightarrow \infty$ :

$$\text{Re}\{\Sigma(i\omega_n)\} \xrightarrow{\omega_n \rightarrow \infty} \Sigma(\infty), \quad (1)$$

while the imaginary part decays to zero.  $\Sigma(\infty)$  captures the static Hartree-Fock contribution from local interactions. We therefore decompose the self-energy as

$$\Sigma(i\omega_n) = \Sigma(\infty) + \Delta\Sigma(i\omega_n), \quad (2)$$

where  $\Delta\Sigma(i\omega_n) \rightarrow 0$  at high frequency. This separation isolates the dynamical correlations in  $\Delta\Sigma$  from the static component  $\Sigma(\infty)$ , each of which can be learned independently.

The dynamical part  $\Delta\Sigma(i\omega)$  is then Fourier transformed to imaginary time and expanded in a Legendre polynomial basis [33],

$$\Delta\Sigma(\tau) = \sum_{\ell=0}^{\ell_{\text{max}}} \sqrt{2\ell+1} P_{\ell}(x(\tau)) \Sigma_{\ell}, \quad (3)$$

where  $x(\tau) = 2\tau/\beta - 1$  and  $P_{\ell}$  are Legendre polynomials. The coefficients  $\Sigma_{\ell}$  decay rapidly with  $\ell$ , providing a compact representation. For example, we find  $\ell_{\text{max}} = 30$  sufficient for Fe and FeO at 5000 K, while NiO at 611 K requires  $\ell_{\text{max}} = 70$  due to finer structure at lower temperature.

In this representation, the Legendre expansion is designed to enforce that  $\Delta\Sigma(i\omega)$  is a smooth function on the Matsubara frequency axis and yields a self-energy with the proper high-frequency properties. Because the Legendre coefficients are real, the learning problem is reduced to predicting a small set of real numbers per orbital and site rather than a noisy complex function on a dense grid. Therefore, we are learning a compact, physically motivated set of coefficients that encode the self-energy under known analytic constraints.

In addition to the self-energy, DMFT calculations require knowledge of the Fermi level  $E_f$  to enforce the total-charge constraint. Small errors in  $E_f$  can lead to discrepancies between impurity and lattice occupancies and thus slow or even prevent convergence. We therefore include  $E_f$  as an additional output of our physics-informed functional.

Given the predicted  $\Sigma^{\text{ML}}(\infty)$  and Legendre coefficients, the approximate self-energy on the Matsubara axis is reconstructed as

$$\Sigma^{\text{ML}}(i\omega_n) = \Sigma^{\text{ML}}(\infty) + \Delta\Sigma^{\text{ML}}(i\omega_n), \quad (4)$$

where  $\Delta\Sigma^{\text{ML}}(i\omega_n)$  is obtained by transforming the Legendre expansion back to the Matsubara axis. Both forward and reverse transformations are performed by the

TRIQS software package [33, 34]. This  $\Sigma^{\text{ML}}$ , together with the predicted  $E_f$ , provides the initial condition for the DMFT self-consistency loop.

Including  $E_f$  as a learned quantity is an essential for achieving substantial speedups. In DFT+DMFT the Fermi level is normally adjusted iteratively so that the total electron number satisfies the charge constraint, and poor initial guesses can severely delay convergence. By treating  $E_f$  on the same footing as  $\Sigma(\infty)$  and the Legendre coefficients, we define a joint functional  $\{\Sigma^{\text{ML}}[\mathcal{S}], E_f^{\text{ML}}[\mathcal{S}]\}$  that maps a crystal structure to a complete, physics-consistent set of input parameters.

To implement this functional, we represent each crystal structure as a periodic atomic graph and approximate  $\{\Sigma^{\text{ML}}[\mathcal{S}], E_f^{\text{ML}}[\mathcal{S}]\}$  with an  $E(3)$ -equivariant graph neural network built using the open-source e3nn software package [35–38]. Atoms are nodes, connected to neighbors within a radial cutoff, and are encoded by learned embeddings of their chemical species and mass. Relative position vectors between neighbors are expanded in spherical harmonics and radial basis functions, so that all edge features and intermediate representations transform as irreducible representations of  $E(3)$ . A small stack of equivariant message-passing layers then builds a symmetry-respecting description of each local environment that is translationally invariant and equivariant under rotations and inversion. Further architectural details are given in the Supplemental Material.

From the final equivariant representation, we construct scalar invariants for prediction. For each inequivalent correlated atom, orbital-specific readout heads map the local features to the static component  $\Sigma(\infty)$  and the truncated set of Legendre coefficients  $\Sigma_\ell$  for that orbital. A separate global readout, obtained by pooling scalar channels over all atoms, yields the Fermi level  $E_f^{\text{ML}}$ . Therefore, a single forward pass of the network maps a crystal structure  $\mathcal{S}$  to  $\Sigma^{\text{ML}}(\infty)$ ,  $\{\Sigma_\ell^{\text{ML}}\}$ , and  $E_f^{\text{ML}}$ ; these are then used to reconstruct  $\Sigma^{\text{ML}}(i\omega_n)$  and provide a fully physics-consistent warm start for the subsequent DFT+DMFT self-consistency cycle.

To assess the accuracy of the physics-informed functional, we first compare its predictions for the self-energy against fully converged DFT+DMFT results on held-out test structures. For Fe and FeO, structural configurations were generated from MD simulations of high-symmetry crystalline prototypes (*e.g.*, hcp/bcc/fcc for Fe, B2 phase for FeO) to ensure coverage of both ordered and disordered environments. 2.5-ps DFT-MD trajectories (0.5 fs timestep) of 4–8 atom cells were generated and representative snapshots were selected by k-medoids clustering in structural fingerprint space [39], yielding 500 configurations in total (100–200 per trajectory). Since the fingerprint represents the chemical environment of each crystal structure, the fingerprint distance allows us to quantify the overall difference in chemical environments between

MAE (eV)	$E_f$	$\Sigma_{z^2}$	$\Sigma_{x^2-y^2}$	$\Sigma_{xz}$	$\Sigma_{yz}$	$\Sigma_{xy}$
Fe	0.217	0.302	0.298	0.315	0.310	0.319
FeO	0.707	0.458	0.341	0.417	0.385	0.408
NiO	0.208	0.198	0.200	0.378	0.3873	0.314

TABLE I. Mean absolute errors of predictions for  $E_f$  and  $\Sigma(\infty)$  orbital components on test set

any two crystal structures. This ensures that we obtain diverse chemical environments for the solver to “learn” in an attempt to aid generalization of results to unseen structures. For NiO we use configurations from our previous study [40]. Full details of dataset generation and selection are provided in the Supplemental Material. We reserve 10% as a held-out test set.

In Fig. 1(a-c), we show the self-energy predictions for 4 random test structures as compared to the self-energies from DFT+DMFT. We find good agreement between predicted and actual self-energies. The errors in the  $\Sigma(i\omega)$  predictions for Fe and FeO were considerably lower than that for NiO. This is likely due to the much lower temperature calculations for NiO, which subsequently lowers Matsubara axis spacing and increases the density of points on the grid.

We also present the errors from the  $\Sigma(\infty)$  predictions as well as the predictions of the Fermi level  $E_f$  in table I. We find in this case, it is instead NiO that provides the lowest error. This could be due to the greater number of training points available for NiO, as well as the similarity in the structures generated as these were sampled directly from perturbations of the atomic structures of certain symmetries. The predictions are reasonable for each compound however, especially as a starting guess for the DFT+DMFT loop. Since further data generation only improves the predictions, one can set up an active learning loop to iteratively improve prediction accuracy.

Figure 1 (d-f) shows the convergence of impurity-lattice occupation difference  $|n_{\text{imp}} - n_{\text{lat}}|$  as a function of DMFT iteration for Fe, FeO, and NiO, averaged over the data for 20 randomly chosen structures. With zero initialization, Fe requires approximately 9 iterations to reach our convergence criterion of  $|n_{\text{imp}} - n_{\text{lat}}| < 0.05$ ; with ML-predicted self-energies, convergence is achieved in 2–3 iterations. Similar speedups are observed for FeO (9 vs. 5 iterations) and NiO (6 vs. 2 iterations). Since each CTQMC iteration dominates the computational cost, this translates directly into a factor of 2–4 reduction in wall-clock time per structure. The learned functional thus acts as a nearly cost-free preconditioner for the DMFT loop, turning the self-energy from a repeated, expensive output into a one-shot, physics-informed initial condition.

Leveraging this acceleration, we performed high-throughput DFT+DMFT calculations on an additional

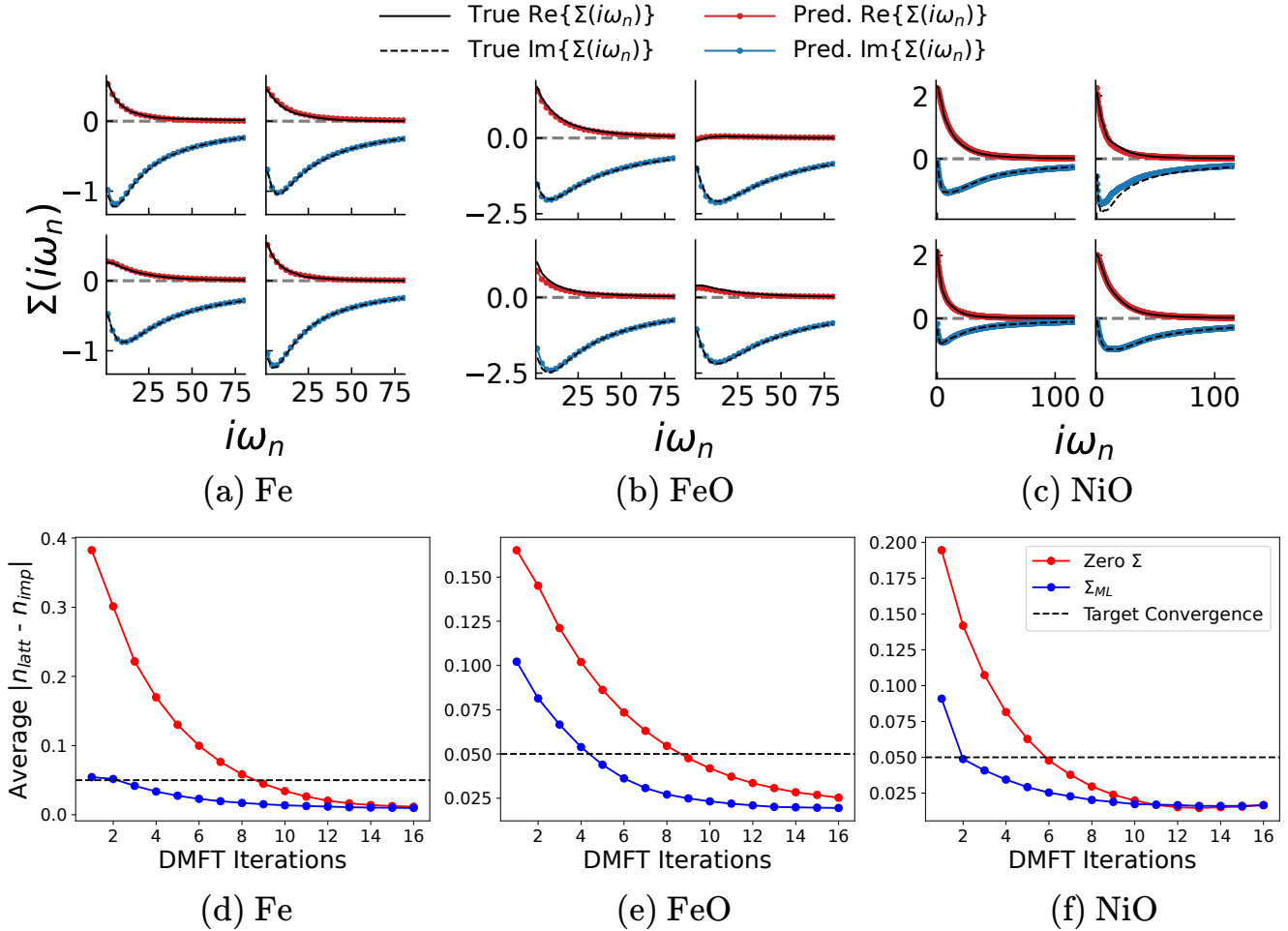


FIG. 1. Top row: Predicted real (red) and imaginary (blue) parts of the self energy vs DMFT (black) self-energies for 4 randomly selected structures in test sets of Fe, FeO and NiO. Bottom row: Convergence for Fe, FeO and NiO versus number of DFT+DMFT iterations.

600 Fe configurations at pressures and temperatures relevant to Earth’s core, increasing the Fe dataset to 1100 configurations with correlated energies and forces. Using all Fe data collected so far, we trained a NequIP-based machine-learned interatomic potential (MLIP) [41, 42], achieving test-set mean absolute errors of 69.2 meV/atom for the energy and 76.7 meV/Å for the forces. Because the reference energies and forces are obtained from a CTQMC impurity solver, the training labels carry finite statistical uncertainty [43]; accordingly, the reported test errors reflect both model discrepancy and an intrinsic noise floor. In the high-temperature regime of interest (*e.g.*,  $T = 5000$  K,  $k_B T \approx 430$  meV), the resulting per-atom energy error remains sub- $k_B T$ , enabling stable large-scale MD and solid–liquid coexistence simulations. To assess sensitivity to the electronic temperature used for DFT+DMFT labeling, we recomputed the electronic free energies for representative Fe configurations at  $T =$

5000 and 6000 K and find changes in relative free-energy differences of  $\leq 6$  meV/atom, well below the MLIP test errors.

We determined melting temperatures using the solid–liquid coexistence method [17], which avoids the hysteresis inherent in single-phase superheating or supercooling approaches. An elongated supercell (9216 atoms) containing coexisting solid (hcp) and liquid regions is equilibrated within the NVE ensemble; if the temperature lies above  $T_m$ , the solid region melts, whereas below  $T_m$  the liquid crystallizes. The phase fractions were monitored using local bond-order analysis [44]. Figure 2 illustrates a representative coexistence configuration at 307.8 GPa: the density profile along the long axis exhibits pronounced oscillations in the crystalline region, characteristic of atomic layering, and a comparatively smooth profile in the liquid region, confirming a well-defined solid–liquid interface. The temperature trace in

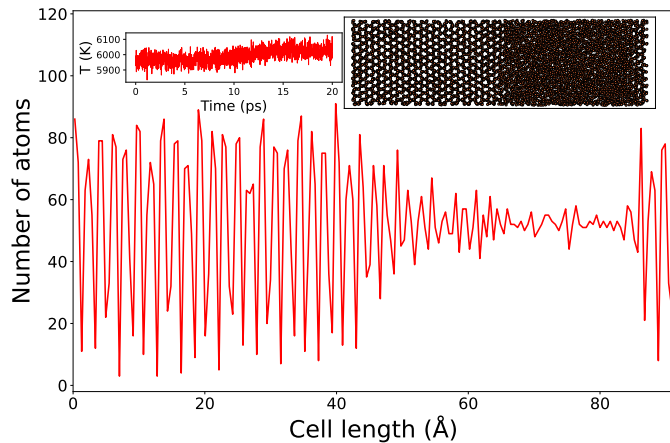


FIG. 2. Density profile along the long axis of simulation cell taken at 20 ps into equilibration for simulation at 307.8 GPa. Shown in the insets are a snapshot of the atomic configuration at 20 ps as well as the temperature variation over the length of the simulation, which stabilizes around 15 ps. The 2 coexistence interfaces can be seen on both sides of the liquid.

the inset shows only moderate fluctuations after 15ps during the NVE run, indicating stable coexistence conditions. Simulations were thermalized for 8 ps and subsequently evolved for 20 ps or 30 ps, depending on phase stabilization, with a 0.5 fs timestep. Pressure was sampled from finite-difference stress calculations including the kinetic contribution, and averaged over the final 5 ps.

Our melting results, spanning 307–352 GPa, is shown in Fig. 3 alongside experimental determinations and prior *ab initio* predictions. The results are well described by a Simon-Glatzel relation [45],

$$T_m = T_0 \left( \frac{P - P_0}{a} + 1 \right)^{1/c}, \quad (5)$$

with  $T_0 = 6167$  K,  $P_0 = 323.1$  GPa,  $a = 298.73$  GPa, and  $c = 2.43$ . At the inner-core boundary pressure of 330 GPa, we obtain  $T_m = 6225 \pm 42$  K, in excellent agreement with the laser-heated diamond anvil cell measurements of Anzellini *et al.* ( $6230 \pm 500$  K) [13] and the ramp-compression experiments of Kraus *et al.* [14]. It is also compatible with the recent shock-compression XAS constraints of Balugani *et al.*, who extrapolate an upper bound of  $6202 \pm 514$  K for Fe at 330 GPa [15]. Our result lies above the resistance-heated DAC determination of Sinmyo *et al.* ( $5500 \pm 220$  K) [46]; however, as noted in Ref. [13], different melting criteria in static experiments can yield systematically different temperatures, and the discrepancy among experiments themselves remains an active area of investigation.

Our agreement with recent experimental constraints also provides insight into why melting predictions for Fe

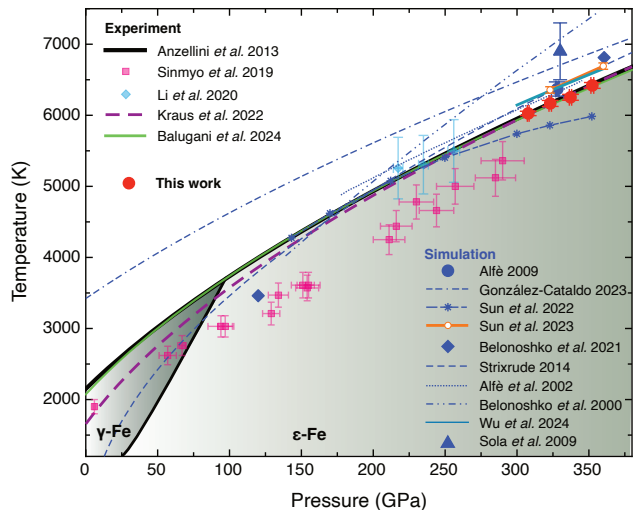


FIG. 3. Full melting curve of Iron as predicted by our 2-phase simulations and compared to data from various experimental [13–15, 46, 50] computational studies [16–25].

at core pressures have remained so dispersed. Most published *ab initio* melting curves based on standard DFT span a broad range and are frequently higher than experimental estimates, with discrepancies reaching several hundred kelvin and an overall scatter approaching  $10^3$  K [16–25]. This sensitivity likely reflects, in part, that commonly used high- $T$  DFT melting workflows dynamical correlations only approximately, thereby missing high-temperature spin fluctuations that contribute to the free energy [10, 12, 47].

Fe at these conditions is paramagnetic, yet thermal spin fluctuations can sustain sizable instantaneous local moments and associated entropy contributions [10, 12, 47]. If these magnetic/electronic excitations are more pronounced in the liquid than in the solid, they increase the entropy of melting and reduce the coexistence temperature through the equilibrium condition  $\Delta G(P, T_m) = 0$ , i.e.  $T_m = \Delta H / \Delta S$ .

DFT+DMFT addresses this limitation by treating the  $3d$  correlations dynamically through the frequency-dependent self-energy  $\Sigma(i\omega_n)$ , capturing quasiparticle renormalization and fluctuating local moments on equal footing. That our melting curve falls within experimental uncertainty while using interaction parameters ( $U, J$ ) adopted from prior DFT+DMFT studies [10, 48, 49] (rather than fitted to melting data) indicates genuine predictive power and is consistent with the view that dynamical correlations account for a substantial part of the long-standing discrepancy between simulation and experiment for Fe at core conditions.

In conclusion, we introduced a physics-informed machine-learning approach that substantially reduces the computational cost of realistic DFT+DMFT calcula-

tions. Rather than directly fitting the noisy Matsubara self-energy as an unconstrained output, we learn a compact representation built from the high-frequency limit and a truncated set of real Legendre coefficients, together with the Fermi level. Implemented with E(3)-equivariant graph neural networks, this provides a physically consistent warm start to the DMFT fixed point and reduces the number of costly impurity iterations by a factor of two to four across Fe, FeO, and NiO. This acceleration turns DFT+DMFT into a practical engine for generating correlated energies and forces at scale. Using the accelerated workflow, we expanded our Fe dataset and trained a NequIP-based MLIP that enables large-scale molecular dynamics for phase equilibrium. Applying solid–liquid coexistence simulations in the 307–352 GPa range, we obtained the melting curve of Fe under core conditions and predict  $T_m = 6225$  K at 330 GPa, in close agreement with recent experimental constraints. More broadly, this approach turns DFT+DMFT into a scalable engine for finite-temperature simulations of correlated materials, with applications ranging from transition-metal compounds to matter under planetary interior conditions.

*Acknowledgements*—This work was supported by the startup funds of the office of the Dean of SASN of Rutgers University-Newark. The authors acknowledge the Office of Advanced Research Computing (OARC) at Rutgers for providing access to the Amarel cluster and associated research computing resources.

*Data Availability*—The software used in prediction of the self-energies and Fermi level has been made available at <https://github.com/Rutgers-ZRG/SigML>

---

\* [li.zhu@rutgers.edu](mailto:li.zhu@rutgers.edu)

- [1] E. Abrahams and G. Kotliar, The metal-insulator transition in correlated disordered systems, *Science* **274**, 1853 (1996).
- [2] M. Imada, A. Fujimori, and Y. Tokura, Metal-insulator transitions, *Rev. Mod. Phys.* **70**, 1039 (1998).
- [3] C. Broholm, R. J. Cava, S. A. Kivelson, D. G. Nocera, M. R. Norman, and T. Senthil, Quantum spin liquids, *Science* **367**, eaay0668 (2020).
- [4] T. E. Lee, S. Gopalakrishnan, and M. D. Lukin, Unconventional magnetism via optical pumping of interacting spin systems, *Phys. Rev. Lett.* **110**, 257204 (2013).
- [5] E. Dagotto, Correlated electrons in high-temperature superconductors, *Rev. Mod. Phys.* **66**, 763 (1994).
- [6] B. Keimer, S. A. Kivelson, M. R. Norman, S. Uchida, and J. Zaanen, From quantum matter to high-temperature superconductivity in copper oxides, *Nature* **518**, 179 (2015).
- [7] G. R. Stewart, Unconventional superconductivity, *Adv. Phys.* **66**, 75 (2017).
- [8] V. I. Anisimov, F. Aryasetiawan, and A. I. Lichtenstein, First-principles calculations of the electronic structure and spectra of strongly correlated systems: the LDA+U method, *J. Phys. Condens. Matter* **9**, 767 (1997).
- [9] Y. Tokura and N. Nagaosa, Orbital physics in transition-metal oxides, *Science* **288**, 462 (2000).
- [10] L. V. Pourovskii, J. Mravlje, A. Georges, S. I. Simak, and I. A. Abrikosov, Electron–electron scattering and thermal conductivity of  $\epsilon$ -iron at earth’s core conditions, *New J. Phys.* **19**, 073022 (2017).
- [11] L. V. Pourovskii, Electronic correlations in dense iron: from moderate pressure to earth’s core conditions, *J. Phys. Condens. Matter* **31**, 373001 (2019).
- [12] O. Y. Vekilova, L. V. Pourovskii, I. A. Abrikosov, and S. I. Simak, Electronic correlations in Fe at earth’s inner core conditions: Effects of alloying with Ni, *Phys. Rev. B* **91**, 245116 (2015).
- [13] S. Anzellini, A. Dewaele, M. Mezouar, P. Loubeyre, and G. Morard, Melting of iron at earth’s inner core boundary based on fast x-ray diffraction, *Science* **340**, 464 (2013).
- [14] R. G. Kraus, R. J. Hemley, S. J. Ali, J. L. Belof, L. X. Benedict, J. Bernier, D. Braun, R. E. Cohen, G. W. Collins, F. Coppari, M. P. Desjarlais, D. Fratanduono, S. Hamel, A. Krygier, A. Lazicki, J. Mcnane, M. Millot, P. C. Myint, M. G. Newman, J. R. Rygg, D. M. Sterbentz, S. T. Stewart, L. Stixrude, D. C. Swift, C. Wehrensberg, and J. H. Eggert, Measuring the melting curve of iron at super-earth core conditions, *Science* **375**, 202 (2022).
- [15] S. Balugani, J. A. Hernandez, N. Sévelin-Radiguet, O. Mathon, V. Recoules, J. J. Kas, D. E. Eakins, H. Doyle, A. Ravasio, and R. Torchio, New constraints on the melting temperature and phase stability of shocked iron up to 270 gpa probed by ultrafast x-ray absorption spectroscopy, *Phys. Rev. Lett.* **133**, 254101 (2024).
- [16] D. Alfè, G. D. Price, and M. J. Gillan, Iron under earth’s core conditions: Liquid-state thermodynamics and high-pressure melting curve from ab initio calculations, *Phys. Rev. B* **65**, 165118 (2002).
- [17] D. Alfè, Temperature of the inner-core boundary of the earth: Melting of iron at high pressure from first-principles coexistence simulations, *Phys. Rev. B* **79**, 060101 (2009).
- [18] A. B. Belonoshko, J. Fu, and G. Smirnov, Free energies of iron phases at high pressure and temperature: Molecular dynamics study, *Phys. Rev. B* **104**, 104103 (2021).
- [19] A. B. Belonoshko, R. Ahuja, and B. Johansson, Quasi–ab initio molecular dynamic study of Fe melting, *Phys. Rev. Lett.* **84**, 3638 (2000).
- [20] F. González-Cataldo and B. Militzer, Ab initio determination of iron melting at terapascal pressures and super-earth core crystallization, *Phys. Rev. Res.* **5**, 033194 (2023).
- [21] E. Sola and D. Alfè, Melting of iron under earth’s core conditions from diffusion monte carlo free energy calculations, *Phys. Rev. Lett.* **103**, 078501 (2009).
- [22] L. Stixrude, Melting in super-earth, *Philos. Trans. R. Soc. A* **372**, 20130076 (2014).
- [23] Y. Sun, F. Zhang, M. I. Mendelev, R. M. Wentzcovitch, and K.-M. Ho, Two-step nucleation of the earth’s inner core, *Proc. Natl. Acad. Sci. U.S.A.* **119**, e2113059119 (2022).
- [24] Y. Sun, M. I. Mendelev, F. Zhang, X. Liu, B. Da, C.-Z. Wang, R. M. Wentzcovitch, and K.-M. Ho, Ab initio melting temperatures of bcc and hcp iron under the earth’s inner core condition, *Geophys. Res. Lett.* **50**, e2022GL102447 (2023).
- [25] F. Wu, S. Wu, C.-Z. Wang, K.-M. Ho, R. M. Wentzcov-

- itch, and Y. Sun, Melting temperature of iron under the earth's inner core condition from deep machine learning, *Geosci. Front.* **15**, 101925 (2024).
- [26] G. Kotliar, S. Y. Savrasov, K. Haule, V. S. Oudovenko, O. Parcollet, and C. A. Marianetti, Electronic structure calculations with dynamical mean-field theory, *Rev. Mod. Phys.* **78**, 865 (2006).
- [27] A. Paul and T. Birol, Applications of DFT + DMFT in materials science, *Annu. Rev. Mater. Res.* **49**, 31 (2019).
- [28] P. Mitra and H. Banerjee, Deep learning-based prediction of self-energies from \*ab initio\* dynamical mean-field theory for real materials with minimal data sets, ChemRxiv 10.26434/chemrxiv-2025-dp7rd (2025).
- [29] X. Dong, E. Gull, and L. Wang, Equivariant neural network for green's functions of molecules and materials, *Phys. Rev. B* **109**, 075112 (2024).
- [30] E. J. Sturm, M. R. Carbone, D. Lu, A. Weichselbaum, and R. M. Konik, Predicting impurity spectral functions using machine learning, *Phys. Rev. B* **103**, 245118 (2021).
- [31] L.-F. Arsenault, A. Lopez-Bezanilla, O. A. von Lilienfeld, and A. J. Millis, Machine learning for many-body physics: The case of the anderson impurity model, *Phys. Rev. B* **90**, 155136 (2014).
- [32] X. Wang, H. T. Dang, and A. J. Millis, High-frequency asymptotic behavior of self-energies in quantum impurity models, *Phys. Rev. B* **84**, 073104 (2011).
- [33] L. Boehnke, H. Hafermann, M. Ferrero, F. Lechermann, and O. Parcollet, Orthogonal polynomial representation of imaginary-time Green's functions, *Phys. Rev. B* **84**, 075145 (2011).
- [34] O. Parcollet, M. Ferrero, T. Ayril, H. Hafermann, I. Krivenko, L. Messio, and P. Seth, TRIQS: A toolbox for research on interacting quantum systems, *Comput. Phys. Commun.* **196**, 398 (2015).
- [35] M. Geiger and T. Smidt, e3nn: Euclidean neural networks, arXiv:2207.09453.
- [36] R. Kondor, Z. Lin, and S. Trivedi, Clebsch-gordan nets: a fully fourier space spherical convolutional neural network, in *Adv. Neural Inf. Process. Syst.*, Vol. 31 (Curran Associates, Inc., 2018).
- [37] N. Thomas, T. Smidt, S. Kearnes, L. Yang, L. Li, K. Kohlhoff, and P. Riley, Tensor field networks: Rotation- and translation-equivariant neural networks for 3d point clouds, arXiv:1802.08219.
- [38] M. Weiler, M. Geiger, M. Welling, W. Boomsma, and T. S. Cohen, 3D steerable CNNs: Learning rotationally equivariant features in volumetric data, in *Adv. Neural Inf. Process. Syst.*, Vol. 31 (Curran Associates, Inc., 2018).
- [39] L. Zhu, M. Amsler, T. Fuhrer, B. Schaefer, S. Faraji, S. Rostami, S. A. Ghasemi, A. Sadeghi, M. Grauzinyte, C. Wolverton, and S. Goedecker, A fingerprint based metric for measuring similarities of crystalline structures, *J. Chem. Phys.* **144**, 034203 (2016).
- [40] R. Rao and L. Zhu, Phase transitions of correlated systems from graph neural networks with quantum embedding techniques, *Phys. Rev. B* **110**, 245111 (2024).
- [41] C. W. Tan, M. L. Descoteaux, M. Kotak, G. de Miranda Nascimento, S. R. Kavanagh, L. Zichi, M. Wang, A. Saluja, Y. R. Hu, T. Smidt, A. Johansson, W. C. Witt, B. Kozinsky, and A. Musaelian, High-performance training and inference for deep equivariant interatomic potentials, arXiv:2504.16068.
- [42] S. Batzner, A. Musaelian, L. Sun, M. Geiger, J. P. Mailoa, M. Kornbluth, N. Molinari, T. E. Smidt, and B. Kozinsky, E(3)-equivariant graph neural networks for data-efficient and accurate interatomic potentials, *Nat. Commun.* **13**, 2453 (2022).
- [43] C. Huang and B. M. Rubenstein, Machine Learning Diffusion Monte Carlo Forces, *J. Phys. Chem. A* **127**, 339 (2023).
- [44] W. Lechner and C. Dellago, Accurate determination of crystal structures based on averaged local bond order parameters, *J. Chem. Phys.* **129**, 114707 (2008).
- [45] Bemerkungen zur schmelzdruckkurve, *Z. Anorg. Allg. Chem.* **178**, 309 (1929).
- [46] R. Sinmyo, K. Hirose, and Y. Ohishi, Melting curve of iron to 290 GPa determined in a resistance-heated diamond-anvil cell, *Earth Planet. Sci. Lett.* **510**, 45 (2019).
- [47] A. V. Ruban, A. B. Belonoshko, and N. V. Skorodumova, Impact of magnetism on Fe under earth's core conditions, *Phys. Rev. B* **87**, 014405 (2013).
- [48] A. G. Gavriliuk, V. V. Struzhkin, A. G. Ivanova, V. B. Prakapenka, A. A. Mironovich, S. N. Aksenov, I. A. Troyan, and W. Morgenroth, The first-order structural transition in NiO at high pressure, *Commun. Phys.* **6**, 23 (2023).
- [49] W.-G. D. Ho, P. Zhang, K. Haule, J. M. Jackson, V. Dobrosavljević, and V. V. Dobrosavljevic, Quantum critical phase of FeO spans conditions of earth's lower mantle, *Nat. Commun.* **15**, 3461 (2024).
- [50] J. Li, Q. Wu, J. Li, T. Xue, Y. Tan, X. Zhou, Y. Zhang, Z. Xiong, Z. Gao, and T. Sekine, Shock melting curve of iron: A consensus on the temperature at the earth's inner core boundary, *Geophys. Res. Lett.* **47**, e2020GL087758 (2020).